CRYSTAL GROWTH & DESIGN

pubs.acs.org/crystal

Article

Magnesium-Based Flux Growth and Structural Relationships of a Large Family of Tetrelide Semimetals

Guillermo Vasquez, Kaya Wei, Eun Sang Choi, Ryan Baumbach, and Susan E. Latturner*

Cite This: *Cryst. Growth Des.* 2020, 20, 2632−2643

Read Online

ACCESS | Metrics & More | Article Recommendations

ABSTRACT: Reactions of tetrels (Tt = Si, Ge, Sn) with divalent alkaline earth or rare earth metals (A = Ca, Sr, Ba, Yb, Eu) in magnesium-rich melts produce a large family of structurally related metal tetrelide compounds with a 2:1 metal to tetrel ratio. The 19 new compounds reported here grow from the flux as large crystals and are structural analogues of hexagonal ternary metal phosphides $Zr_2Fe_{12}P_7$, $Ho_5Ni_{19}P_{12}$, $Ho_6Ni_{20}P_{13}$, or $Ho_{20}Ni_{66}P_{43}$. Trends in element substitutions on the various sites in the structures were investigated. The charge-balanced $(A/Mg)_2Tt$ compositions result in semimetallic behavior, and the complex structures and heavy element incorporation yield low thermal conductivity. $Ba_5Eu_{2.85}Mg_{16.15}Si_{12}$, $Ba_5Yb_{2.26}Mg_{16.74}Si_{12}$, and $Ba_5Sr_{2.92}Mg_{16.08}Si_{12}$ have room temperature thermal conductivities of 2−3 W/mK and Seebeck coefficients of +130 μV/K, −75 μV/K, and −150 μV/K respectively. These materials are promising for thermoelectric applications at high temperatures. Incorporation of europium results in compounds exhibiting antiferromagnetic coupling forces between Eu^{2+} ions.

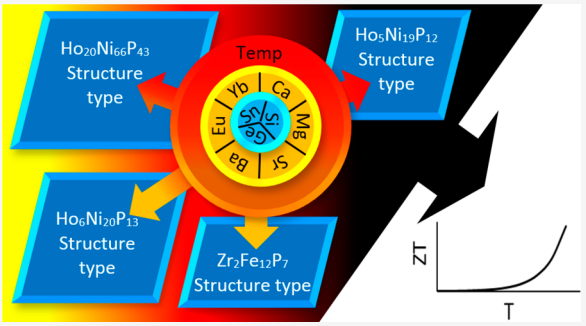

INTRODUCTION

Thermoelectric compounds are materials that generate a voltage when a temperature gradient is applied, making them useful for converting waste heat into electricity. The thermoelectric efficiency of a material is determined by its thermoelectric figure of merit ZT ($ZT = [S^2/\rho\kappa]T$, where κ = thermal conductivity, ρ = electrical resistivity, S = Seebeck coefficient, and T is temperature). Optimization is difficult given that S, ρ, and κ are interrelated and are all dependent upon carrier concentration. Narrow band gap semiconductors or semimetals tend to have the best balance of ρ and S for obtaining a high ZT value. Phases with complex crystal structures and heavy elements often have low thermal conductivity (κ), which further increases the ZT value; Zintl phases are of increasing interest for this reason.[1] Zintl phases are salt-like compounds that form when highly electropositive alkali, alkaline earth, or rare earth metals react with main group metalloids. The metalloids accept the electrons from the metals and may also form M−M bonds to fill their valence shells, resulting in anions that are charge balanced by surrounding metal cations. As a result of being charge-balanced, these compounds are typically small band gap semiconductors. Metal silicides such as $Ba_{1.9}Ca_{2.4}Mg_{9.7}Si_7$, $Ba_8Al_{14}Si_{31}$, and $Mg_2(Si,Sn)$ are of interest since they are composed of earth abundant and environmentally friendly elements, unlike Bi_2Te_3 and PbSe; the former contains tellurium, deemed to be a near-critical material by the United States government, and the latter incorporates toxic Pb.[1−5]

Metal fluxes have proven to be a useful medium for the synthesis of new silicide phases. Flux reactions involve the use of a low melting metal as a solvent; refractory elements such as silicon dissolve in the molten metal and react at temperatures well below their melting point, allowing for the formation of complex intermetallics and the growth of large crystals.[6] Metal silicide compounds grown from flux reactions include β-$FeSi_2$, MnSi and FeSi(Al) as potential photoelectric materials, as well as $CrSi_2$, $MnSi_{1.7}$, $Mg_2(Si,Sn)$, and $Ba_8Al_{14}Si_{31}$ as potential thermoelectric materials.[7−11,2,5] In our previous work, we synthesized the new silicide Zintl phases $Ba_{20}Yb_{4.7}Mg_{61.3}Si_{43}$, $Ba_5Yb_{2.29}Mg_{16.71}Si_{12}$, $Ba_6Yb_{1.84}Mg_{18.16}Si_{13}$, and $Ba_2Yb_{0.88}Mg_{11.12}Si_7$ from reactions of barium, ytterbium, and silicon in a Mg/Al flux. These compounds form in the $Ho_{20}Ni_{66}P_{43}$, $Ho_5Ni_{19}P_{12}$, $Ho_6Ni_{20}P_{13}$, and $Zr_2Fe_{12}P_7$ structure types, respectively; the Ho (or Zr) sites are occupied by barium cations, the Ni (or Fe) sites by a mixture of Yb and Mg cations, and the P sites are occupied by silicide anions leading to an overall 2:1 charge-balanced composition $(Ba/Yb/Mg)_2Si$.[12] The complex structures, site mixing, and incorpo-

Received: January 5, 2020
Revised: March 11, 2020
Published: March 13, 2020

https://dx.doi.org/10.1021/acs.cgd.0c00012
Cryst. Growth Des. 2020, 20, 2632−2643

Table 1. Synthesis Ratios, Heating Profiles, and Products Produced from Reactions in Mg/Al Flux

reactants	reaction ratio (mmol)	heating profile[a]	products	CCDC no.
(Mg/Al)/Sr/Yb/Ge	(15/15)/2.5/0.5/3	b	$Sr_2Yb_{0.81}Mg_{11.19}Ge_7$	1958414
(Mg/Al)/Sr/Yb/Sn	(15/15)/1.5/1.5/3	b	$Sr_2Yb_{2.32}Mg_{9.68}Sn_7$	1958415
(Mg/Al)/Eu/Yb/Si	(15/15)/2.5/1/3	b	$Eu_2Yb_{1.11}Mg_{10.89}Si_7$	1958416
(Mg/Al)/Sr/Eu/Si	(15/15)/2.5/1.5/3	b	$Sr_5Eu_{1.39}Mg_{17.61}Si_{12}$	1958417
(Mg/Al)/Sr/Eu/Ge	(15/15)/2/1/3	b	$Sr_{3.93}Eu_{3.07}Mg_{17}Ge_{12}$	1958418
(Mg/Al)/Eu/Yb/Si	(15/15)/1/1/3	b	$Eu_5Yb_{1.98}Mg_{17.02}Si_{12}$	1958419
(Mg/Al)/Ba/Yb/Si/Ge	(21/9)/1.25/0.25/1.5/0.25	b	$Ba_5Yb_{1.91}Mg_{17.09}Si_{10.01}Ge_{1.99}$	1958420
(Mg/Al)/Ba/Yb/Si/Sn	(21/9)/1.25/0.25/1.5/0.75	c	$Ba_5Yb_{1.66}Mg_{17.34}Si_{11.68}Sn_{0.32}$	1958422
(Mg/Al)/Ba/Yb/Si/Ge	(21/9)/1.25/0.25/1.0/0.75	c	$Ba_5Yb_{1.38}Mg_{17.62}Si_{6.47}Ge_{5.53}$	1958425
(Mg/Al)/Ba/Yb/Ge	(15/15)/2/1/3	b	$Ba_5Yb_{2.37}Mg_{16.63}Ge_{12}$	1958426
(Mg/Al)/Ba/Eu/Si	(15/15)/2/0.5/3	b	$Ba_5Eu_{2.85}Mg_{16.15}Si_{12}$	1958427
(Mg/Al)/Ba/Eu/Si/Ge	(15/15)/2.5/0.5/2.25/0.75	d	$Ba_5Eu_{2.43}Mg_{16.57}Si_{7.58}Ge_{4.42}$	1958428
(Mg/Al)/Sr/Ba/Si	(15/15)/1.5/1.5/3	b	$Ba_5Sr_{2.92}Mg_{16.08}Si_{12}$	1958429
(Mg/Al)/Sr/Yb/Ge	(15/15)/1.5/1.5/3	b	$Sr_5Yb_{2.49}Mg_{16.51}Ge_{12}$	1958567
(Mg/Al)/Ba/Eu/Si	(29/1)/1/0.25/2.75	e	$Ba_6Eu_3Mg_{17}Si_{13}$	1958430
(Mg/Al)/Sr/Eu/Si	(15/15)/2.5/0.5/3	b	$Ba_{20}Eu_{5.51}Mg_{60.49}Si_{43}$	1958431
(Mg/Al)/Ca/Ba/Si	(21/9)/0.25/1.25/1.5	b	$Ba_{20}Mg_{66}Si_{43}$	1958432
(Mg/Al)/Ba/Yb/Si/Ge	(21/9)/1.25/0.25/0.25	b	$Ba_{20}Yb_{0.76}Mg_{65.24}Si_{37.92}Ge_{5.08}$	1958433
(Mg/Al)/Ba/Yb/Ge	(29/1)/1.25/0.25/1.5	b	$Ba_{20}Yb_{2.62}Mg_{63.38}Ge_{43}$	1958434

[a]Heating profiles. [b]RT to 950 °C in 10 h, hold at 950 °C for 10 h, 950−750 °C in 80 h. [c]RT to 950 °C in 10 h, hold at 950 °C for 10 h, 950−725 °C in 35 h. [d]RT to 950 °C in 5 h, hold at 950 °C for 5 h, 950−725 °C in 80 h. [e]RT to 950 °C in 10 h, hold at 950 °C for 5 h, 950−750 °C in 40 h.

ration of heavy elements indicate that the compounds have the potential for low thermal conductivity and may be of interest as thermoelectric materials.

We have expanded this work to explore reactions of other electropositive divalent metals (A = Ca, Sr, Ba, Eu, Yb) with different tetrel elements (Tt = Si, Ge, Sn) in Mg/Al flux mixtures. In this report, we present 19 new compounds that have resulted from these reactions, which just scratches the surface of the versatility of this chemistry. All of these products feature a 2:1 ratio of divalent cations to tetrelide anions and are thus charge-balanced and can be represented with a general formula $(A/Mg)_2Tt$. All exhibit complex hexagonal structures that are analogous to those of a series of rare earth transition metal phosphides. These new compounds are all semimetallic, and the silicides are air-stable. Magnetic characterization of the europium compounds confirm that this metal is divalent in these phases and indicates antiferromagnetic coupling forces between Eu^{2+} ions. The complex structures, site mixing, and incorporation of heavy elements indicate that these materials may exhibit useful thermoelectric behavior. This hypothesis was tested by collecting resistivity, thermal conductivity, and Seebeck coefficient data for three compounds ($Ba_5Eu_{2.85}Mg_{16.15}Si_{12}$, $Ba_5Yb_{2.26}Mg_{16.74}Si_{12}$, and $Ba_5Sr_{2.92}Mg_{16.08}Si_{12}$).

EXPERIMENTAL PROCEDURES

Synthesis. The elemental reactants were used as received: magnesium and aluminum slugs (99.95% and 99.99%, Alfa Aesar); ytterbium chunks (99.9%, Alfa Aesar); europium chunks (99%, Alfa Aesar); barium rod (99+%, Alfa Aesar); silicon powder (99+%, Strem), germanium powder (99.9%, Alfa Aesar); strontium chunks (99%, Strem); and tin powder (99.8%, Alfa Aesar). An excess of magnesium/aluminum flux was used, most commonly in a 15:15 mmol ratio of the elements; this melts at 450 °C. Smaller amounts of the other reactants were used, in the range of 3−4 mmol for the tetrel element, and 0.5−3 mmol of the divalent metals; see Table 1. For example, $Ba_5Eu_{2.85}Mg_{16.15}Si_{12}$ was synthesized using a Mg/Al/Si/Ba/Eu ratio of 15:15:3:2:0.5 mmol. These elements were loaded into a stainless steel crucible under argon. The crucible was sealed shut by arc-welding under argon and then placed in a silica tube and flame-sealed under a vacuum (30 mTorr). The ampule was heated from room temperature to 950 °C in 10 h, held at 950 °C for 10 h, and cooled to 750 °C in 80 h. The reaction ampule was then removed from the furnace, inverted, and centrifuged for 1 min to decant the remaining Mg/Al melt. The steel crucible was cut open and the crystals adhered to the walls of the crucible were scraped out. This produced $Ba_5Eu_{2.85}Mg_{16.15}Si_{12}$ in roughly 50% yield, based on Eu as a limiting reagent. In some reactions, byproducts of $BaMgAlSi_2$ (with $BaAl_4$ structure type) were observed. Other $(A/Mg)_2Tt$ phases were synthesized in a similar fashion, with variations on the reaction ratio and the heating profile explored to optimize yield and crystal growth; see Table 1.

Elemental Analysis. Products were analyzed by SEM-EDS using a FEI Nova 400 NanoSEM with energy dispersive spectroscopy (EDS) capabilities. Samples of product crystals were mounted onto aluminum pucks using double-sided carbon tape and analyzed using a 30 kV acceleration voltage. The surface of the pucks was completely covered with carbon tape to eliminate artifacts produced by the aluminum. SEM-EDS data for the compounds generally compared well to the results of single crystal structure refinements; for instance, EDS of $Sr_5Yb_{2.49}Mg_{16.51}Ge_{12}$ indicated Sr/Yb/Mg/Ge mole percentages of 16(1): 8(1): 44(2): 32(2), which is in agreement with its X-ray structure. The surface of the crystals typically showed residual flux droplets in some areas, so measurements were taken on cleaved samples or on surfaces where no flux was present. The data showed no incorporation of elements from the stainless steel crucible. The presence of aluminum was indicated in trace amounts no higher than 2−3% in some samples (these spectra were compared to data for Si wafers to confirm that the Al peaks were not artifacts).

Diffraction Studies. Samples were examined under a microscope to select crystals for diffraction studies. Suitable pieces were cut from larger crystals and were mounted in Dual-Thickness MicroLoops (MiTeGen Loop/Mount) using Parabar oil. Single-crystal X-ray diffraction data were collected at 293 K (or at 200 K for air sensitive samples), using either a Bruker APEX 2 CCD diffractometer with a Mo Kα radiation source or a Rigaku XtaLAB Synergy-S diffractometer equipped with a HyPix-6000HE Hybrid Photon Counting (HPC) detector and dual Mo and Cu microfocus sealed X-ray source. Absorption corrections were applied to the data sets using the SADABS program. Refinement of the structures were performed using the SHELXTL package.[13,14] Crystallographic information for

https://dx.doi.org/10.1021/acs.cgd.0c00012
Cryst. Growth Des. 2020, 20, 2632−2643

Table 2. Crystallographic Data and Collection Parameters for Representative $(A/Mg)_2Tt$ Compounds of Each Structure Type

	$Eu_2Yb_{1.11}Mg_{10.89}Si_7$	$Ba_5Yb_{1.91}Mg_{17.09}Si_{10.01}Ge_{1.99}$	$Ba_6Eu_3Mg_{17}Si_{13}$	$Ba_{20}Yb_{0.76}Mg_{65.24}Si_{37.92}Ge_{5.08}$
structure type	$Zr_2Fe_{12}P_7$	$Ho_5Ni_{19}P_{12}$	$Ho_6Ni_{20}P_{13}$	$Ho_{20}Ni_{66}P_{43}$
space group	*P*-6	*P*-62*m*	*P*-6	$P6_3/m$
a (Å)	10.9910(7)	14.761(1)	15.482(1)	27.966(4)
c (Å)	4.3250(3)	4.5046(3)	4.5082(3)	4.4919(6)
V (Å^3)	452.47(7)	849.99(13)	935.80(15)	3042.4(9)
Z	1	1	1	1
calc density (g/cm^3)	3.513	3.630	3.652	3.219
temp (K)	293	293	293	293
radiation type	Mo Kα	Mo Kα	Mo Kα	Mo Kα
μ (mm^{-1})	13.35	13.29	11.86	8.89
reflections	837	839	1708	3524
parameters	49	51	84	149
R_1, wR_2 (all data)	0.0178, 0.0331	0.0125, 0.0261	0.0104, 0.0252	0.0584, 0.0695
R_1, wR_2 ($I > 2\sigma(I)$)	0.0162, 0.0331,	0.0123, 0.0261	0.0104, 0.0252	0.0391, 0.0695
$\Delta\rangle_{max}$, $\Delta\rangle_{min}$ (e Å^{-3})	0.58, −0.68	0.71, −0.54	0.70, −0.66	1.69, −1.25

Table 3. An Overview of Known $(A/Mg)_2Tt$ Phases with Hexagonal Ternary Metal Phosphide ($R_{n(n-1)}T_{(n+1)(n+2)}P_{n(n+1)+1}$ Family) Structure Types

composition	*a* (Å)	*c* (Å)	reference
$Zr_2Fe_{12}P_7$ structure type (n = 2)			
Hexagonal, *P*-6			
$Sr_{2.2}Mg_{11.8}Ge_7$	11.064(1)	4.356(1)	17
$Ba_2Mg_{12}Ge_{7.33}$	11.217(5)	4.402(2)	18
$Eu_{2.47}Mg_{11.53}Ge_7$	11.093(1)	4.351(1)	19
$Eu_2Yb_{1.11}Mg_{10.89}Si_7$	10.9910(7)	4.3250(3)	This work
$Ba_{1.2}Sr_{0.9}Mg_{11.9}Ge_7$	11.0636(16)	4.3709(6)	3
$Ba_2Yb_{0.88}Mg_{11.12}Si_7$	11.0830(6)	4.4150(3)	12
$Sr_2Yb_{0.81}Mg_{11.19}Ge_7$	11.0887(11)	4.3675(4)	This work
$Ba_{1.9}Ca_{2.4}Mg_{9.7}Si_7$	11.196(2)	4.4595(9)	3
$Sr_2Yb_{2.32}Mg_{9.68}Sn_7$	11.8098(7)	4.6606(3)	This work
$Ho_5Ni_{19}P_{12}$ structure type (n = 3, variant)			
Hexagonal, *P*-62*m*			
$Eu_{5.09}Mg_{17.91}Ge_{13}$	14.5194(8)	4.3890(3)	20
$Eu_5Yb_{1.98}Mg_{17.02}Si_{12}$	14.5259(18)	4.3800(6)	This work
$Sr_5Eu_{1.39}Mg_{17.61}Si_{12}$	14.553(2)	4.4023(7)	This work
$Sr_{6.3}Mg_{16.7}Ge_{13}$	14.711(1)	4.4459(3)	21
$Eu_{7.29}Mg_{15.71}Si_{12.73}$	14.621(3)	4.4073(9)	22
$Eu_{7.15}Mg_{15.85}Si_{13}$	14.6356(14)	4.4111(6)	23
$Sr_{6.3}Mg_{16.7}Si_{13}$	14.640(1)	4.4313(3)	21
$Ba_5Mg_{18}Si_{13}$	14.606(3)	4.4818(3)	21
$Ba_5Mg_{18}Ge_{13}$	14.727(1)	4.5093(3)	21
$Ba_5Yb_{1.91}Mg_{17.09}Si_{10.01}Ge_{1.99}$	14.761(1)	4.5046(3)	This work
$Sr_5Yb_{2.49}Mg_{16.51}Ge_{12}$	14.7671(12)	4.4449(4)	This work
$Ba_5Yb_{1.38}Mg_{17.62}Si_{6.47}Ge_{5.53}$	14.767(24)	4.5059(7)	This work
$Ba_5Yb_{1.66}Mg_{17.34}Si_{11.68}Sn_{0.32}$	14.7811(7)	4.5134(2)	This work
$Sr_{3.93}Eu_{3.07}Mg_{17}Ge_{12}$	14.7915(20)	4.4568(6)	This work
$Eu_{7.9}Mg_{16.07}Ge_{12}$	14.7930(6)	4.4519(3)	20
$Ba_5Yb_{2.26}Mg_{16.73}Si_{12}$	14.8223(8)	4.5174(3)	12
$Ba_5Eu_{2.85}Mg_{16.15}Si_{12}$	14.857(2)	4.5225(5)	This work
$Ba_5Yb_{2.37}Mg_{16.63}Ge_{12}$	14.8606(17)	4.5305(5)	This work
$Ba_5Eu_{2.43}Mg_{16.57}Si_{7.58}Ge_{4.42}$	14.8716(7)	4.5307(2)	This work
$Ba_5Sr_{2.92}Mg_{16.08}Si_{12}$	14.9289(2)	4.5502(1)	This work
$Ho_6Ni_{20}P_{13}$ structure type (n = 3)			
Hexagonal, *P*-6			
$Ba_6Yb_{1.84}Mg_{18.16}Si_{13}$	15.4554(11)	4.5046(3)	16
$Ba_6Eu_3Mg_{17}Si_{13}$	15.4819(11)	4.5082(3)	This work
$Ho_{20}Ni_{66}P_{43}$ structure type (n = 6)			
Hexagonal, $P6_3/m$			
$Ba_{20}Yb_{4.70}Mg_{61.30}Si_{43}$	27.928(4)	4.4808(6)	12
$Ba_{20}Eu_{5.51}Mg_{60.49}Si_{43}$	27.9876(31)	4.4914(5)	This work
$Ba_{20}Mg_{66}Si_{43}$	27.805(4)	4.4741(6)	This work
$Ba_{20}Yb_{0.76}Mg_{65.24}Si_{37.92}Ge_{5.08}$	27.9659(39)	4.4919(6)	This work
$Ba_{20}Yb_{2.62}Mg_{63.38}Ge_{43}$	28.188(3)	4.5316(6)	This work

representative compounds of the four observed structure types are shown in Table 2. Additional crystallographic data for all samples are available as CIF files from the Cambridge Crystallographic Data Centre under the CCDC file numbers shown in Table 1. Powder X-ray diffraction data were collected on ground bulk samples of flux-grown products using a PANalytical X-Pert PRO with a Cu Kα radiation source. The resulting pattern was compared to the calculated pattern based on the single crystal structure.

Thermoelectric Measurements. Single crystals of $Ba_5Eu_{2.85}Mg_{16.15}Si_{12}$, $Ba_5Yb_{2.26}Mg_{16.74}Si_{12}$, and $Ba_5Sr_{2.92}Mg_{16.08}Si_{12}$ were mounted on a custom-designed sample holder using Ag paste with the orientation such that the current and the thermal gradient

https://dx.doi.org/10.1021/acs.cgd.0c00012
Cryst. Growth Des. 2020, 20, 2632−2643

were along the *c*-axis direction. The thermal conductivity was measured using the conventional one-heater-two-thermometer method.[15] Two Cernox bare chip sensors were used for the thermometer, and a polished thin metal chip resistor was used for the heater. A stepwise increasing heater power (d*P*) to the chip resistor generated a stepwise thermal gradient across the sample. The temperature gradient (d*T*) and the corresponding thermoelectric voltage (d*V*) were simultaneously measured when d*T* was stabilized at each heater power. The thermal conductivity and the Seebeck coefficient were obtained by the relations, $\kappa \approx dP/dT$ and $S = dV/dT$, respectively. The four-probe electrical resistivity was measured by applying constant current when the heater power was zero. The polarity of the current was reversed to eliminate the thermal emf.

Magnetic Susceptibility Measurements. Temperature dependent magnetic susceptibility data for $Ba_5Eu_{2.85}Mg_{16.15}Si_{12}$ and $Eu_5Yb_{1.98}Mg_{17.02}Si_{12}$ were measured used a Quantum Design MPMS SQUID magnetometer. Samples were prepared by placing a large single crystal between pieces of Kapton tape with the *c*-axis of the crystals placed parallel to the magnetic field; this strip of tape was then placed in a plastic sample holder for insertion into the magnetometer. Field-cooled (FC) and zero-field cooled (ZFC) measurements were carried out over a temperature range of 1.8−300 K with an applied field of 1000 G ($Ba_5Eu_{2.85}Mg_{16.15}Si_{12}$) and 15 000 G ($Eu_5Yb_{1.98}Mg_{17.02}Si_{12}$).

RESULTS AND DISCUSSION

Synthesis. Reactions of tetrels (Si, Ge, Sn) with heavy divalent metals (Ca, Sr, Ba, Eu, Yb) in magnesium-based fluxes produce complex new tetrelide Zintl phases as well-formed crystals. This synthesis method offers the possibility of forming a vast number of $(A/Mg)_2Tt$ compounds, allowing for cation mixing on the A and Mg sites and tetrel mixing on the Tt sites. The large amount of magnesium in the flux promotes the formation of magnesium-rich products. This likely prevents the formation of known AMgTt phases with the orthorhombic TiNiSi structure type; for instance, SrMgSi or BaMgSi are not seen. This aspect of the chemistry was further manipulated by modifying the Mg/Al flux ratio. While a 15:15 mmol ratio was initially used, this did allow for occasional formation of $BaAl_{4-x}(Mg/Si)_x$ compounds. To prevent this, higher Mg content fluxes were explored (such as 21:9 or 29:1 Mg/Al mmol ratios), which did minimize/eliminate these byproducts. It is notable however that pure magnesium was not effective as a flux to grow these tetrelides; some small amount of Al is needed.[12] It is not known whether the presence of aluminum works to better solubilize the tetrel element, or whether it is needed to stabilize the products. The final fate of the aluminum is also not certain; quenching experiments reported for reactions of Ba, Yb, and Si in Mg/Al flux indicate that the remaining flux at the end of the reaction is largely a Mg/Ba mixture, with much of the aluminum having reacted with the surface of the steel crucible to form a $Ni_{1-x}Fe_xAl$ compound embedded in the walls.[16] However, in some reaction systems, EDS analysis does indicate incorporation of small amounts of aluminum into the $(A/Mg)_2Tt$ product; this was only seen for Eu-containing compounds and was never in amounts higher than 3%. For instance, analysis of $Ba_5Eu_{2.85}Mg_{16.15}Si_{12}$ indicated atomic ratios of 14(2)% Ba, 10(2)% Eu, 40(1)% Mg, 3(1)% Al, and 33(1)% Si. It is not clear whether this is a flux coating or inclusion, or an indication of actual Al incorporation into the product (possibly mixing on a Mg or Si site, which would unfortunately be unresolvable in the X-ray diffraction studies), so the compositions are presented without aluminum in them. A summary of hexagonal $(A/Mg)_2Tt$ compounds reported thus far—both discovered in this work as well as reported in the literature—is shown in Table 3. The ternary compounds reported by the Nesper and Corbett groups were grown from high temperature reactions of stoichiometric mixtures.[17−21,23]

All these products form in the Mg/Al flux as rod or needle-shaped silver crystals with hexagonal cross sections; see Figure 1. The $Ho_5Ni_{19}P_{12}$ structure type compounds all grow as very

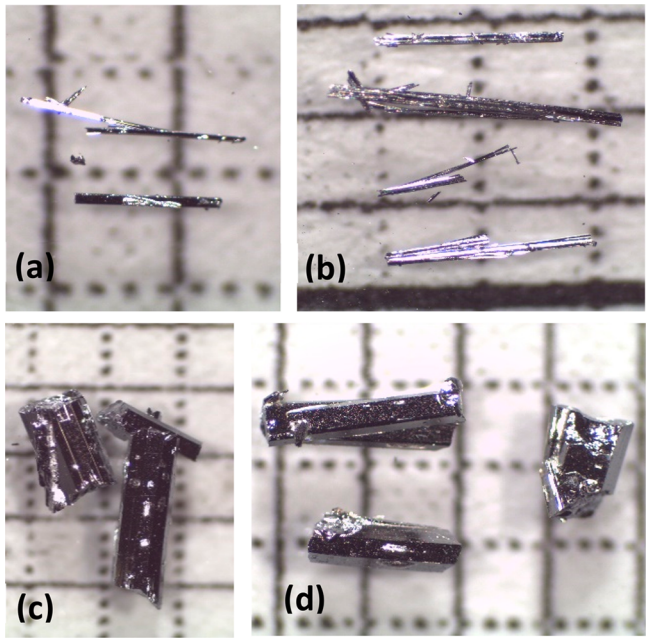

Figure 1. Microscope images on 1 mm grid paper of crystals of various hexagonal $(A/Mg)_2Tt$ compounds grown from Mg/Al flux. (a) $Eu_2Yb_{1.11}Mg_{10.89}Si_7$, (b) $Ba_{20}Yb_{0.76}Mg_{65.24}Si_{37.92}Ge_{5.08}$, (c) $Eu_5Yb_{1.98}Mg_{17.02}Si_{12}$, (d) $Ba_6Eu_3Mg_{17}Si_{13}$.

large single crystals with lengths and widths in the millimeter range, however; all the $Ho_{20}Ni_{66}P_{43}$ type phases grow as needles with much smaller widths. The crystals are brittle and cleave readily. All silicides (and mixed-anion compounds with Si as their predominant anion) are air-stable. Both Ge and Sn compounds are very air sensitive with the Ge analogues oxidizing within a few days, while the Sn compounds oxidize within a few hours. Samples with Ge and Si mixing are more resistive to oxidization; compounds with higher Ge concentrations oxidize more quickly than those with lower concentrations. The trend in reaction yield is similar to that of air stability; reactions with silicon typically resulted in a high yield of product (50−60% yield for $Ba_5Eu_{2.85}Mg_{16.15}Si_{12}$; PXRD data shown in Figure 2), whereas germanium and tin reactions produced smaller yields (10% or lower) of products.

The outcomes of reactions were also dependent on heating profile. Our *in situ* study on the Ba/Yb/Mg/Si system indicated that $Ba_{20}Yb_{4.70}Mg_{61.30}Si_{43}$ forms in reactions cooled from 950 to 650 °C in 10 h, whereas $Ba_5Yb_{2.26}Mg_{16.73}Si_{12}$ forms if an identical reaction is cooled more slowly.[16] This is borne out by the fact that our commonly used longer heating profile (used because it tends to form larger crystals, within the mm range) preferentially grows the $Ho_5Ni_{19}P_{12}$-type phases, with $Ho_{20}Ni_{66}P_{43}$ structure compounds occurring as minor byproducts. The crystals grow to much smaller dimensions with a shorter heating profile.

Structures. The $(A/Mg)_2Tt$ products are all structural analogues of ternary metal phosphides. A large number of

https://dx.doi.org/10.1021/acs.cgd.0c00012
Cryst. Growth Des. 2020, 20, 2632−2643

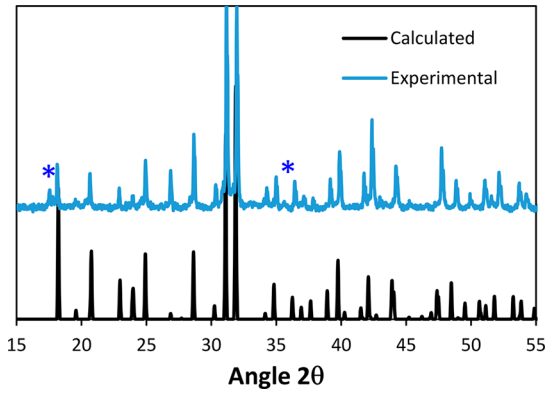

Figure 2. Powder X-ray diffraction data for product of reaction of Ba, Eu, and Si in Mg/Al flux (Mg/Al/Si/Ba/Eu in 15/15/3/2/0.5 mmol ratio). Calculated pattern derived from the $Ba_5Eu_{2.85}Mg_{16.15}Si_{12}$ crystal structure is in black, while the data for the powdered product are in blue. Diffraction peaks from secondary phases indicated by asterisks.

$R_xT_yP_z$ compounds (R = rare earth, T = transition metal) have been reported that feature a 2:1 metal to phosphorus ratio, with phosphorus sites surrounded by nine metal sites in tricapped trigonal prismatic coordination. These $P@(R,T)_9$ units pack together in a variety of different patterns, many of which form homologous series such as $R_{n(n-1)}T_{(n+1)(n+2)}P_{n(n+1)+1}$.[24,25] As a result, all of these phosphides have hexagonal symmetry with similar *c*-axis lengths. All the flux-grown $(A/Mg)_2Tt$ compounds are analogues of the $Zr_2Fe_{12}P_7$, $Ho_5Ni_{19}P_{12}$, $Ho_6Ni_{20}P_{13}$, and $Ho_{20}Ni_{66}P_{43}$ structure types; all four structures are comprised of face-sharing $Tt@(A/Mg)_9$ tricapped trigonal prisms (resulting in very similar *c*-axis lengths in the 4.35−4.55 Å range, see Table 3). The structural series (and its intergrowth compounds) can also be viewed as being comprised of triangular assemblies of atoms that increase in size and packing complexity as *n* rises.[24,25] A diagram of these four structure types is shown in Figure 3 to highlight the dependence of the size of repeating triangular subunits on *n*. It is notable that no tetrelide analogue of the *n* = 4 structure ($(La,Ce)_{12}Rh_{30}P_{21}$ type)[24] or the *n* = 5 structure (hypothetical, no known example) has yet been found.

$Zr_2Fe_{12}P_7$-type Analogues. The $Zr_2Fe_{12}P_7$ structure type, exemplified by $Eu_2Yb_{1.11}Mg_{10.89}Si_7$, is shown in Figure 4. Our

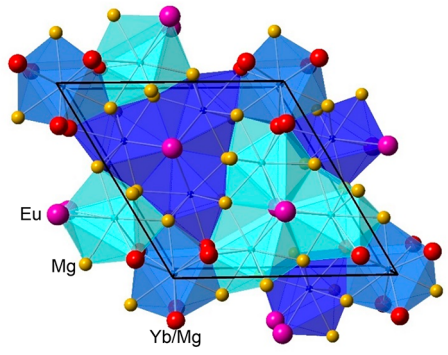

Figure 4. $Eu_2Yb_{1.11}Mg_{10.89}Si_7$ structure ($Zr_2Fe_{12}P_7$ type, space group *P*-6) viewed along the *c*-axis. Mg, Eu, and Yb/Mg sites shown as yellow, fuchsia, and red spheres, respectively. The three unique Si sites are shown as tricapped trigonal prisms in three shades of blue.

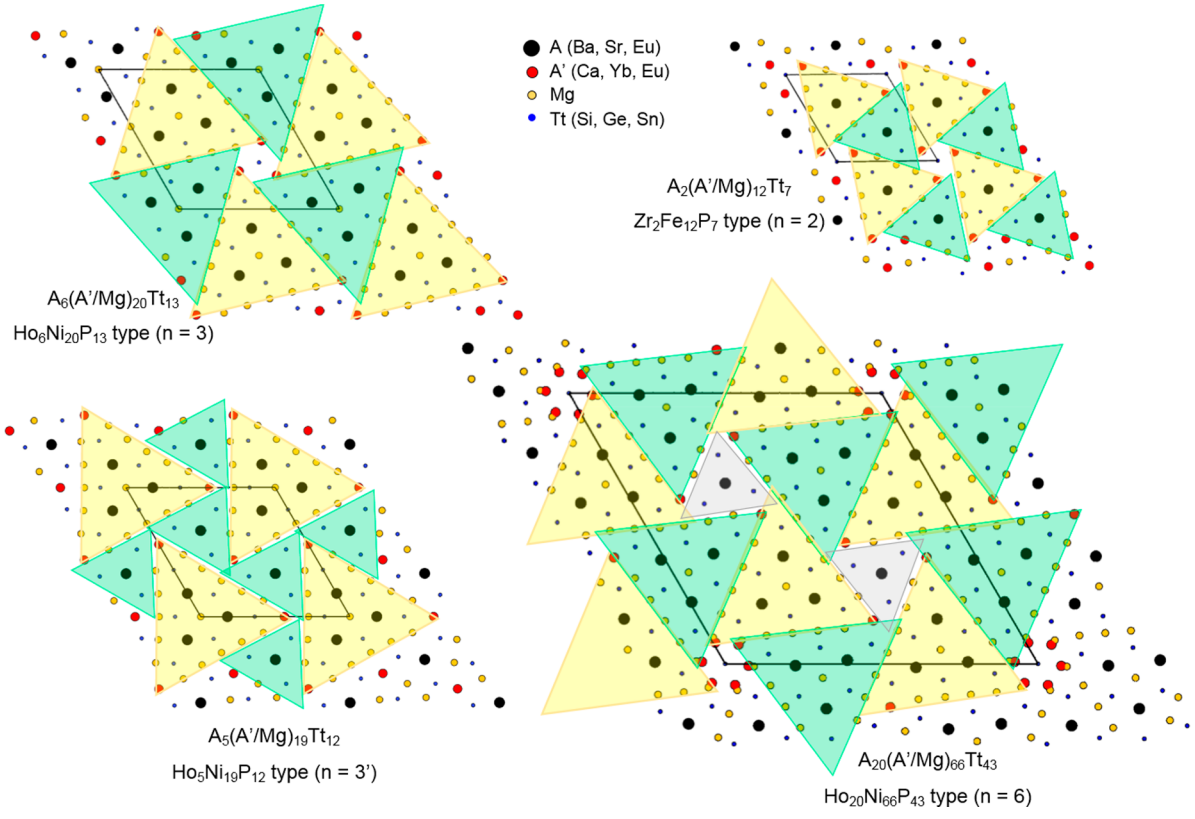

Figure 3. Four structures observed for $(A/Mg)_2Tt$ compounds synthesized in this work, viewed down the *c*-axes. Triangular patterns of increasing size and complexity are highlighted.

https://dx.doi.org/10.1021/acs.cgd.0c00012
Cryst. Growth Des. 2020, 20, 2632−2643

initial report on isostructural $Ba_{1.9}Ca_{2.4}Mg_{9.7}Si_7$ indicated promising thermoelectric properties at high temperatures (a ZT of 0.4 at 900 K), which triggered our interest in further investigating this system, exploring Yb incorporation, and introducing more cation and anion mixing. $A_2Mg_{12}Ge_7$ analogues with A = Sr, Ba, and Eu were previously reported by the Corbett and Nesper groups.[17−19]

The large alkaline earth and rare earth cations (Sr, Ba, or Eu) occupy the zirconium sites of the $Zr_2Fe_{12}P_7$ structure type with no indication of mixing with smaller elements. This A site is coordinated by six tetrelide atoms; the Eu−Si bond length (3.367(2)−3.351(2) Å) in $Eu_2Yb_{1.11}Mg_{10.89}Si_7$ is within range of the Eu−Si distances seen in $Eu_{7.15}Mg_{15.85}Si_{13}$ (2.964−3.862 Å).[23] Similarly, the Sr−Ge bond distances in $Sr_2Yb_{0.81}Mg_{11.19}Ge_7$ (3.408(5)−3.391(5) Å), and the Sr−Sn bond distances in $Sr_2Yb_{2.32}Mg_{9.68}Sn_7$ (3.5835(4)−3.6031(4) Å) are respectively within range of previously reported Sr−Ge bond distances found in $Sr_5Mg_{19}Ge_{12}$ and $Sr_{6.3}Mg_{16.7}Ge_{13}$ (3.405−3.459 Å), and Sr−Sn distances found in SrMgSn and Sr_2Sn (3.331−3.993 Å).[17,26,27]

The magnesium atoms occupy the iron sites of $Zr_2Fe_{12}P_7$. In the quaternary variants $(A/A'/Mg)_2Tt$ with A = large cation (Ba, Eu) and A′ = small cation (Ca, Yb, or Sr), there is mixing of the A′ element onto the 3*k* magnesium sites. The mixing is significant in the compounds containing ytterbium, with ratios of 37%Yb/63%Mg for $Eu_2Yb_{1.11}Mg_{10.89}Si_7$ and 27%Yb/73%Mg for $Sr_2Yb_{0.81}Mg_{11.19}Ge_7$. The $Sr_2Yb_{2.32}Mg_{9.68}Sn_7$ and $Ba_{1.9}Ca_{2.4}Mg_{9.7}Si_7$ phases have very similar mixing (77%Yb/23%Mg and 77%Ca/23%Mg respectively). Mixing is limited in $Ba_{1.2}Sr_{0.9}Mg_{11.9}Ge_7$ (3%Sr/97%Mg), likely due to the large difference in ionic radii between strontium and magnesium.

Definitive trends relating ionic radii and unit cell size cannot be derived for analogues because interdependent substitutions often happen on multiple sites. For instance, a contraction in the unit cell, from *a* = 11.196(2) Å (in $Ba_{1.9}Ca_{2.4}Mg_{9.7}Si_7$) to *a* = 11.0830(6) Å (in $Ba_2Yb_{0.85}Mg_{11.15}Si_7$) occurs when Ca is replaced with Yb. However, this may be accounted for not by the different sizes of Ca^{2+} and Yb^{2+}, but by the difference in the amount of magnesium present in the sample. The increased amount of magnesium cations in the $Ba_2Yb_{0.85}Mg_{11.15}Si_7$ phase may be causing the phase to contract in comparison to the $Ba_{1.9}Ca_{2.4}Mg_{9.7}Si_7$ phase. Similarly, substitution on the large element sites is often accompanied by changing ratios on other sites, as is seen going from $Ba_2Yb_{0.85}Mg_{11.15}Si_7$ to $Eu_2Yb_{1.11}Mg_{10.89}Si_7$; the *a*- and *c*-axes decrease from 11.0830(6) Å and 4.4150(3) Å for the barium analogue to 10.9910(7) Å and 4.3250(3) Å for the europium compound, but the Yb/Mg ratio is also changed. Some general trends are apparent upon tetrelide substitution, however. The majority of the known analogues (see Table 3) are germanides. As expected, a contraction of unit cell parameters is observed when comparing similar germanides and silicides (exemplified by $Ba_2Mg_{12}Ge_7$ and $Ba_2Yb_{0.85}Mg_{11.15}Si_7$). On the other hand, if germanium is replaced with tin, an expansion in the unit cell parameters occurs. The *a*- and *c*-axes increase significantly from 11.088(11) Å and 4.3685(4) Å in $Sr_2Yb_{0.81}Mg_{11.19}Ge_7$ to 11.8098(7) Å and 4.6606(3) Å in $Sr_2Yb_{2.32}Mg_{9.68}Sn_7$.

$Ho_5Ni_{19}P_{12}$-type Analogues. The $Ho_5Ni_{19}P_{12}$ structure type, exemplified $Ba_5Yb_{1.91}Mg_{17.09}Si_{10.01}Ge_{1.99}$, is shown in Figure 5. This structure type was the most commonly observed for $(A/Mg)_2Tt$ products of these Mg/Al flux reactions. Ternary analogues were initially reported by Slabon and Nesper, who isolated "$A_{5+x}Mg_{18-x}Tt_{13}$" compounds with A = Sr, Ba, Eu and Tt = Si or Ge (six compounds, included in Table 3). These were made from arc melting of stoichiometric element mixtures.[20] Perhaps because of this different synthesis technique, the Nesper group reported incorporation of a tetrel atom on a 1b Wyckoff site typically expected to be occupied by Mg, resulting in a 5:18:13 ratio instead of the expected 5:19:12 composition.[21] Synthesis in excess Mg-rich flux produces compounds with the latter ratio. These phases, as well as cation and anion-mixed variants, can be grown readily as large rod-like crystals from Mg/Al flux reactions.

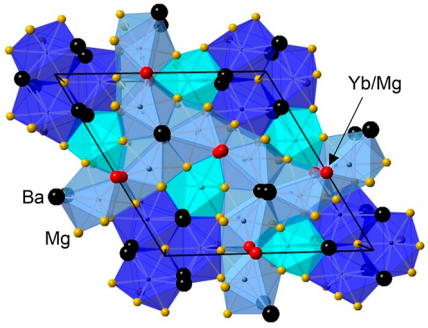

Figure 5. $Ba_5Yb_{1.9}Mg_{16.10}Si_{10.01}Ge_{1.99}$ structure ($Ho_5Ni_{19}P_{12}$ type, space group *P*-62*m*) viewed along the *c*-axis. Ba sites are in black, Yb/Mg mixed sites are in red, Mg sites are in yellow, and Si/Ge mixed sites are shown as tricapped trigonal prisms in three shades of blue.

This structure has three crystallographically unique tetrelide sites, two unique rare earth sites and five unique magnesium sites. The rare earth sites are occupied by the largest rare earth or alkaline earth elements: Ba, Sr, or Eu. These 2d and 3f Wyckoff sites are coordinated by a trigonal prism of six tetrelides, with bond distances comparable to those reported in other compounds. For instance, the $Ba_5Eu_{2.85}Mg_{16.15}Si_{12}$, $Ba_5Yb_{1.66}Mg_{17.34}Si_{11.68}Sn_{0.32}$, and $Ba_5Sr_{2.92}Mg_{16.08}Si_{12}$ phases have Ba−Si bond lengths in the 3.493(1)−3.538(2) Å range, which are similar to previously reported Ba−Si distances (3.3729−3.7653 Å) found in $BaSi_2$.[27] In $Sr_{3.93}Eu_{3.07}Mg_{17}Ge_{12}$ and $Sr_5Yb_{2.49}Mg_{16.51}Ge_{12}$ the Sr−Ge bond lengths fall within the range of 3.4195(6)−3.4704(8) Å and are comparable to previously reported Sr−Ge bond lengths found in SrCaGe and SrMgGe (3.249−3.607).[28,26]

In all of the quaternary $A_5(A'/Mg)_{19}Tt_{12}$, the fourth element (A′ = Yb, Eu or Sr) mixes onto one specific magnesium 3*g* Wyckoff site. The site ranges from slightly magnesium-rich (54−55% Mg/45−46% rare earth in $Ba_5Yb_{1.38}Mg_{17.62}Si_{6.47}Ge_{5.53}$ and $Sr_5Eu_{1.39}Mg_{17.61}Si_{12}$) to significantly rare earth-rich (with $Ba_5Eu_{2.85}Mg_{16.15}Si_{12}$ and $Ba_5Yb_{2.37}Mg_{16.63}Ge_{12}$ having respective ratios of 95%Eu/5% Mg and 83%Yb/17%Mg in this site). An elongation of the bond distances around this 3g site is observed, as one would expect. In the $Ba_5Eu_{2.85}Mg_{16.15}Si_{12}$ phase for instance, the distance from the mixed Eu/Mg site to neighboring silicon sites (3.0222(2)−3.209(1) Å) is on the shorter side for Eu−Si distances (2.964−3.862 Å) reported in $Eu_{7.15}Mg_{15.85}Si_{13}$, but are longer than the Mg−Si bonds reported for Mg_2Si (2.7657 Å).[23,29]

The ability to isolate compounds of this structure type readily and in high yield allowed for exploration of anion mixing. We previously reported the formation of the $Ba_5Yb_{2.26}Mg_{16.73}Si_{12}$ phase. In this work, we were able to synthesize a germanide analogue, as well as several mixed Si/Ge phases. The unit cell of the phase expands as the amount of

https://dx.doi.org/10.1021/acs.cgd.0c00012
Cryst. Growth Des. 2020, 20, 2632−2643

germanium substitution increases, with the *a*-axis increasing from 14.761(1) Å to 14.767(2) Å to 14.861(2) Å going from $Ba_5Yb_{1.91}Mg_{17.09}Si_{10.01}Ge_{1.99}$ to $Ba_5Yb_{1.38}Mg_{17.62}Si_{6.47}Ge_{5.53}$ to $Ba_5Yb_{2.37}Mg_{16.63}Ge_{12}$. The unit cell of the $Ba_5Yb_{2.26}Mg_{16.73}Si_{12}$ phase cannot be directly compared with the germanide analogues, since single crystal data for the germanide phases were collected at low temperature under nitrogen flow to prevent oxidation.

In the $Ba_5(Yb/Mg)_{19}Tt_{12}$ phases with Tt = Si/Ge mixtures, the Tt mixing was evenly distributed across all three tetrelide sites. Refinement of the diffraction data for $Ba_5Yb_{1.91}Mg_{17.09}Si_{10.01}Ge_{1.99}$ indicates germanium contents in the range of 13−18% for all three sites. The germanium content on these sites rises to 44−47% for $Ba_5Yb_{1.38}Mg_{17.62}Si_{6.47}Ge_{5.53}$. The ratios of germanium to silicon reagents used to synthesize the $Ba_5Yb_{1.91}Mg_{17.09}Si_{10.01}Ge_{1.99}$ and $Ba_5Yb_{1.38}Mg_{17.62}Si_{6.47}Ge_{5.53}$ were (0.25 mmol Ge/1.5 mmol Si) and (0.75 mmol Ge/1.0 mmol Si), which are respectively 14% and 43% germanium ratio in tetrelide reactant. This indicates a strong correlation with the amount of germanium used as a reactant and the amount incorporated on all the tetrelide sites. The bond lengths of the tetrelide sites with neighboring magnesium sites for both compounds are in the range 2.630(6)−2.923(17) Å, comparable to previously reported Mg−Si bond lengths found in Mg_2Si (2.7657 Å) and $Ba_{1.9}Ca_{2.4}Mg_{9.7}Si_7$ (2.734(1)−2.903(1) Å), although the longest bond length (2.923(17) Å) is more comparable to the longest Mg−Ge bond lengths (2.582−2.919 Å) found in $Sr_5Mg_{19}Ge_{12}$ and $Sr_{6.3}Mg_{16.7}Ge_{13}$ phases.[29,3,17,16]

Substitution of silicon with tin was also explored. A 0.25 mmol Sn/1.5 mmol Si reactant ratio (14% Sn, 86% Si) was used to synthesize $Ba_5Yb_{1.66}Mg_{17.34}Si_{11.68}Sn_{0.32}$, but the resulting ratios of these elements in the product are 3% Sn and 97% Si. This indicates a possible maximum threshold of tin incorporation onto the tetrelide sites, as might be expected due to the very different radii of these elements. Only one tetrelide site appears to incorporate tin. This 3f site was refined as a mixture of 11% Sn/89% Si. The distance between the mixed site and neighboring Mg (2.767(2)−2.872(2) Å) is slightly shorter than Mg−Sn bond distances (2.975 Å) reported for BaMgSn but are slightly elongated compared to Mg−Si bond distances (2.7657 Å) and (2.647(21)−2.887(14) Å) reported in Mg_2Si and $Ba_{1.9}Ca_{2.4}Mg_{9.7}Si_7$ respectively.[29,3]

$Ho_6Ni_{20}P_{13}$-type Analogues. The $Ho_6Ni_{20}P_{13}$ structure type, exemplified by $Ba_6Eu_3Mg_{17}Si_{13}$, is shown in Figure 6.

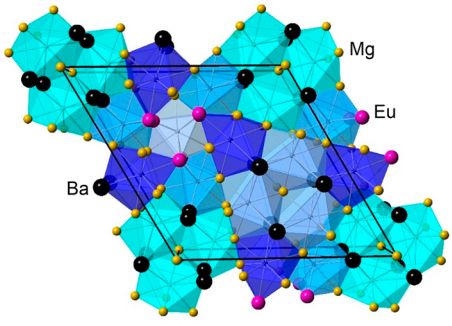

Figure 6. $Ba_6Eu_3Mg_{17}Si_{13}$ structure ($Ho_6Ni_{20}P_{13}$ type, space group *P*-6) viewed along the *c*-axis. Ba sites are in black, Eu sites are in fuchsia, Mg sites are in yellow, and Si sites are shown as tricapped trigonal prisms in various shades of blue.

Only two products with this structure type were found from Mg/Al flux reactions: $Ba_6(A'/Mg)_{20}Si_{13}$ with A′ = Yb, Eu (see Table 3). This structure has five unique tetrelide sites, two unique large rare earth sites and seven unique magnesium/small rare earth sites. $Ba_6Yb_{1.84}Mg_{18.16}Si_{13}$ was previously reported by our group.[16] Replacing the Yb by Eu yields an analogue with a slight expansion of the unit cell from *a* = 15.4554(11) Å and *c* = 4.5046(3) Å (in $Ba_6Yb_{1.84}Mg_{18.16}Si_{13}$) to *a* = 15.4819(11) Å and *c* = 4.5082(3) Å (in $Ba_6Eu_3Mg_{17}Si_{13}$); this is to be expected since europium has a larger ionic radius than ytterbium and magnesium, and the substitution level of A′ for Mg is higher in the europium compound.

In the $Ba_6Eu_3Mg_{17}Si_{13}$ phase, barium occupies the holmium sites of the parent structure. The Ba−Si bond lengths (3.466(1)−3.553(2) Å) are within range of previously reported Ba−Si bond lengths (3.3729−3.7653 Å) reported in $BaSi_2$.[26] Of the seven unique magnesium sites, magnesium fully occupies six of them, while europium occupies the seventh, a 3k Wyckoff site. No mixing on the magnesium and europium sites was observed. The Eu−Si bond distance (2.937(2)−3.098(2) Å) is within range of previously reported Eu−Si bond distances (2.964−3.862 Å in $Eu_{7.15}Mg_{15.85}Si_{13}$).[20] The Mg−Si bond distance is shorter (2.695(2)−2.896(3) Å) and is within range of Mg−Si bond distances (2.647(21)−2.887(14) Å) previously seen in $Ba_{1.9}Ca_{2.4}Mg_{9.7}Si_7$.[3]

$Ho_{20}Ni_{66}P_{43}$-type Analogues. The $Ho_{20}Ni_{66}P_{43}$ structure type, exemplified by $Ba_{20}Yb_{0.76}Mg_{65.24}Si_{37.92}Ge_{5.08}$, is shown in Figure 7. This structure type is the most complex of the four

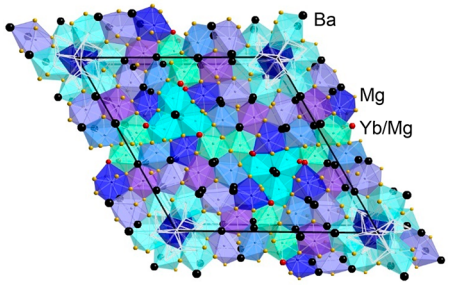

Figure 7. $Ba_{20}Yb_{0.76}Mg_{65.24}Si_{37.92}Ge_{5.08}$ structure ($Ho_{20}Ni_{66}P_{43}$ type, space group $P6_3/m$) viewed along the *c*-axis. Ba sites are in black, Yb/Mg mixed sites are in red, Mg sites are in yellow, and Si and Si/Ge mixed sites are shown as tricapped trigonal prisms in various shades of blue.

observed in this work, and analogues cannot be made using stoichiometric synthesis. Our previous *in situ* studies indicated the metastability of this structure. In the Ba/Yb/Mg/Si system, $Ba_{20}Yb_{4.7}Mg_{61.3}Si_{43}$ crystallized at 640 °C from a reaction mixture that was cooled quickly through its metastable solubility region, whereas an identical reaction cooled slowly led to crystallization of $Ba_5Yb_{2.26}Mg_{16.73}Si_{12}$ at 800 °C.[16] Further work on other A/A′/Mg/Tt systems produced analogues of this structure type with A = Ba, A′ = Yb or Eu, and Tt = Si, Ge (see Table 3). The ternary variant $Ba_{20}Mg_{66}Si_{43}$ has the smallest unit cell parameters (*a* = 27.807(2) Å and *c* = 4.5191(3) Å). Substituting some of the Mg for larger Yb (forming $Ba_{20}Yb_{4.70}Mg_{61.30}Si_{43}$ with *a* = 27.928(4) Å) or Eu (forming $Ba_{20}Eu_{5.51}Mg_{60.49}Si_{43}$ with *a* = 27.9876(31) Å) expands the size of the unit cell as expected.

https://dx.doi.org/10.1021/acs.cgd.0c00012
Cryst. Growth Des. 2020, 20, 2632−2643

This structure has 8 unique tetrelide sites, 4 barium sites, and 12 Mg or Mg/A′ sites. In all four analogues, barium atoms occupy the holmium sites of the parent structure; analogues were not found with other large divalent cations. The $Ba_{20}Eu_{5.51}Mg_{60.49}Si_{43}$, $Ba_{20}Mg_{66}Si_{43}$, and $Ba_{20}Yb_{0.76}Mg_{65.24}Si_{37.92}Ge_{5.08}$ phases all have Ba−Si bond lengths spanning from 3.417(1)−3.557(1) Å; these are within range of previously reported Ba−Si bond lengths of 3.3729−3.7653 Å found in $BaSi_2$.[24] For the $Ba_{20}Yb_{2.62}Mg_{63.38}Ge_{43}$ phase, the Ba−Ge bond lengths (3.436(7)−3.5860(7) Å) are within range of previously reported Ba−Ge bond lengths in $Ba_5Mg_{18}Ge_{13}$ (3.255−3.796 Å) and in $BaGe_2$ (3.410−3.786 Å).[18,30]

Of the 12 nickel sites of the parent $Ho_{20}Ni_{66}P_{43}$ structure, 10 are occupied by magnesium and 2 (6h sites) by a Mg/A′ mixture in these compounds. In $Ba_{20}Eu_{5.51}Mg_{60.49}Si_{43}$ occupancies of these two mixed sites were refined as 65% Eu/35% Mg and 54% Eu/46% Mg. The addition of europium causes a slight elongation of the Mg−Si bond distance into the range 2.922(2)−3.126(1) Å compared to previously reported Mg−Si bonds (2.734(1)−2.903(1) Å) but is within range of previously reported Eu−Si bonds (2.964−3.862 Å) found in $Eu_{7.15}Mg_{15.85}Si_{13}$.[20] Similar elongation is seen around the mixed sites in the ytterbium-containing analogues. For instance, in $Ba_{20}Yb_{0.76}Mg_{65.24}Si_{37.92}Ge_{5.08}$ the two sites refine as 9.6% Yb/90.4% Mg and 7.1% Yb/92.9% Mg, with Mg−Si/Ge bond lengths between 2.847(2)−3.137(2) Å; these are within range of previously reported Yb−Ge (3.083−3.213 Å) and Yb−Si (2.889−3.038 Å) bond distance reported in YbMgGe and $YbSi_2$.[31,32]

The eight phosphorus sites of the parent structure are fully occupied by tetrelides except for the disordered 2a site, which is half occupied (a feature characteristic of the $Ho_{20}Ni_{66}P_{43}$ structure type, and discussed in further detail in our work on $Ba_{20}Yb_{4.7}Mg_{61.3}Si_{43}$).[12] Substitution of silicon for germanium was explored; this expands the unit cell size as expected (with the *a*-axis increasing from 27.928(4) Å to 27.9659(39) Å to 28.188(3) Å going from $Ba_{20}Yb_{4.70}Mg_{61.30}Si_{43}$ to $Ba_{20}Yb_{0.76}Mg_{65.24}Si_{37.92}Ge_{5.08}$ to $Ba_{20}Yb_{2.62}Mg_{63.38}Ge_{43}$). In $Ba_{20}Yb_{0.76}Mg_{65.24}Si_{37.92}Ge_{5.08}$, silicon/germanium mixing occurs relatively evenly in seven of the eight silicon sites; each of these six sites has 11−14% Ge. The addition of germanium on the silicon sites causes a slight elongation of the Mg−Si/Ge bond distances (2.587(7)−2.953(3) Å), compared to previously reported Mg−Si bond distances (2.734(1)−2.903(1) Å) found in $Ba_{1.9}Ca_{2.4}Mg_{9.7}Si_7$ but are within range of previously reported Mg−Ge bond (2.582−2.919 Å) lengths found in $Sr_5Mg_{19}Ge_{12}$ and $Sr_{6.3}Mg_{16.7}Ge_{13}$ phases (2.582−2.919 Å).[3,18,19]

Magnetic Properties of Rare Earth Containing Analogues. Previous magnetic susceptibility studies on $Ba_2Yb_{0.9}Mg_{11.1}Si_7$, $Ba_5Yb_2Mg_{17}Si_{12}$, $Ba_6Yb_{1.84}Mg_{18.16}Si_{13}$, and $Ba_{20}Yb_5Mg_{61}Si_{43}$ show they are all Pauli paramagnetic, indicating that ytterbium is divalent in $(A/Yb/Mg)_2Tt$ compounds.[12] Initial magnetic susceptibility studies on $(Eu/A/Mg)_2Si$ phases indicate that europium is also divalent in these materials. Data were collected for $Ba_5Eu_{2.85}Mg_{16.15}Si_{12}$ and $Eu_5Yb_{1.98}Mg_{17.02}Si_{12}$ from 2 to 300 K at applied fields of 1000 and 15 000 G respectively, and are shown in Figure 8 and Figure 9. For $Ba_5Eu_{2.85}Mg_{16.15}Si_{12}$, the Curie−Weiss fit of the paramagnetic region above 50 K indicates a moment per Eu ion of 8.2 μ_B, which is slightly higher than the theoretical moment of 7.94 μ_B expected for Eu^{2+}. The Weiss constant θ was found to be −0.15 K, indicating very weak antiferromagnetic coupling forces are present. Very similar values were found from the Curie−Weiss fit of the data for $Eu_5Yb_{1.98}Mg_{17.02}Si_{12}$, which has a moment per Eu ion of 8.3 μ_B, and a Weiss constant θ = −0.17 K. Both compounds therefore contain divalent europium ions which are too far apart to exhibit strong magnetic coupling forces. Both of these phases have the $Ho_5Ni_{19}P_{12}$ structure type. The Eu^{2+} cations in $Eu_5Yb_{1.98}Mg_{17.02}Si_{12}$ occupy the holmium sites, with a minimum distance between these sites of 4.3800(6) Å. In $Ba_5Eu_{2.85}Mg_{16.15}Si_{12}$, on the other hand, the europium cations are randomly distributed on Mg/Eu mixed sites. While it is possible that some of these Eu^{2+} cations could be in adjacent sites, these are located 4.5388 Å apart. These structural features are consistent with the very low Weiss constants and with the fact that no long-range ordering is observed down to low temperatures. There is some slight deviation from Curie−Weiss behavior starting below 4 K for both compounds, with $Eu_5Yb_{1.98}Mg_{17.02}Si_{12}$ exhibiting weak splitting between field-cooled and zero-field cooled data below 2 K, but no distinct cusp indicative of magnetic ordering. This is in contrast to the reported behavior of $Eu_{7.2}Mg_{15.8}Si_{13}$, a variant of the $Ho_5Ni_{19}P_{12}$ structure type which has Eu^{2+} cations on both the holmium sites and one of the nickel sites. This compound exhibits ferromagnetic ordering at close to 10 K, likely facilitated by the higher concentration of europium and short distance of 4.323 Å between the 2c and 3f sites.[21]

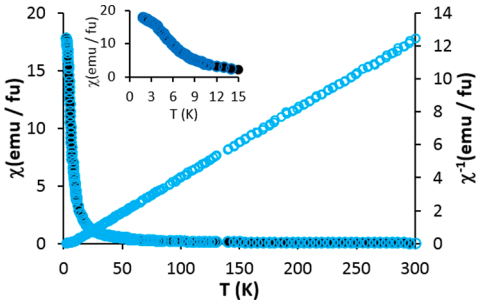

Figure 8. Magnetic susceptibility data for $Ba_5Eu_{2.85}Mg_{16.15}Si_{12}$. Data were collected under an applied field of 1000 G applied parallel to the *c*-axis of a single crystal. Zero-field cooled data are indicated by closed black dots, and FC data are indicated by open colored dots. Inverse susceptibility curves are plotted from the ZFC data. The inset shows slight deviation from Curie−Weiss behavior below 4 K.

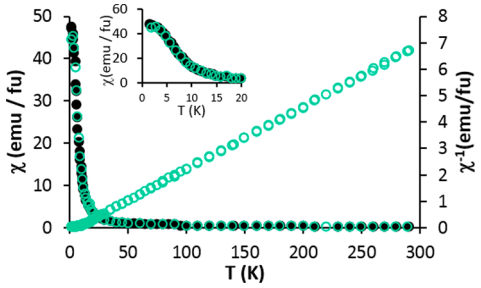

Figure 9. Magnetic susceptibility data for $Eu_5Yb_{1.98}Mg_{17.02}Si_{12}$, collected under an applied field of 15 000 G applied parallel to the *c*-axis of a single crystal. Zero-field cooled data are indicated by closed black dots, and FC data are indicated by open colored dots. Inverse susceptibility curves are plotted from the ZFC data. The inset shows slight deviation from Curie−Weiss behavior below 4 K.

Thermoelectric Properties of $Ba_5(A'/Mg)_{19}Si_{12}$ with A′ = Yb, Eu, and Sr. To characterize thermoelectric behavior,

https://dx.doi.org/10.1021/acs.cgd.0c00012
Cryst. Growth Des. 2020, 20, 2632−2643

low temperature measurements of electrical resistivity ρ, thermal conductivity κ, and Seebeck coefficient S were carried out on crystals of three $(Ba/A'/Mg)_2Si$ phases with the $Ho_5Ni_{19}P_{12}$ structure type. From these data, the thermoelectric figure of merit ($ZT = S^2T/\rho\kappa$) can be calculated. Comparison of the data allows us to observe the effects of substituting Yb for Eu or Sr. Band structure calculations previously carried out on model compound $Ba_5Yb_2Mg_{17}Si_{12}$ indicate a pseudogap at E_F; it is therefore expected that all of these compounds should exhibit semimetallic or poor metal behavior.[12]

The data for $Ba_5Yb_{2.26}Mg_{16.74}Si_{12}$ are shown in Figure 10. Slight kinks in the data near 270 K are likely due to the freezing of trace water vapor. The resistivity has a weak dependence on temperature, with ρ rising from 0.80 mΩ·cm to 1.00 mΩ·cm as the temperature rises from 2 K to 300 K. This is indicative of a metallic or semimetallic behavior. The magnitude of resistivity is comparable to that of other semimetals such as $Ba_{1.9}Ca_{2.4}Mg_{9.7}Si_7$ (0.80 mΩ·cm) and $Mg_2Si_{0.6}Sn_{0.4}$ (0.065 mΩ·cm) at room temperature.[3,33] The thermal conductivity is extremely low, ranging from 2−4 W/mK. This is comparable to the values observed for $Ba_{1.9}Ca_{2.4}Mg_{9.7}Si_7$, and lower than that seen for fluorite structure Mg_2Si, which has ρ = 3 to 3−3.5 W/mK in the same temperature range.[3,34,35] The rise in thermal conductivity and a maximum at 14 K is the expected result of the gradual reduction of lattice vibrations as the temperature drops. Since phonons are no longer scattered by these vibrations, a rise in thermal conductivity at low temperature is typically observed in most crystalline materials. The negative sign of the Seebeck coefficient S indicates that the majority of charge carriers in $Ba_5Yb_{2.26}Mg_{16.74}Si_{12}$ are electrons. The magnitude rises from close to zero at low temperature to −75 μV/K at 300 K. This is significantly higher than metallic compounds such as ZrCoSb and HfCoSb (both have $S \approx -10$ μV/K at 300 K).[36]

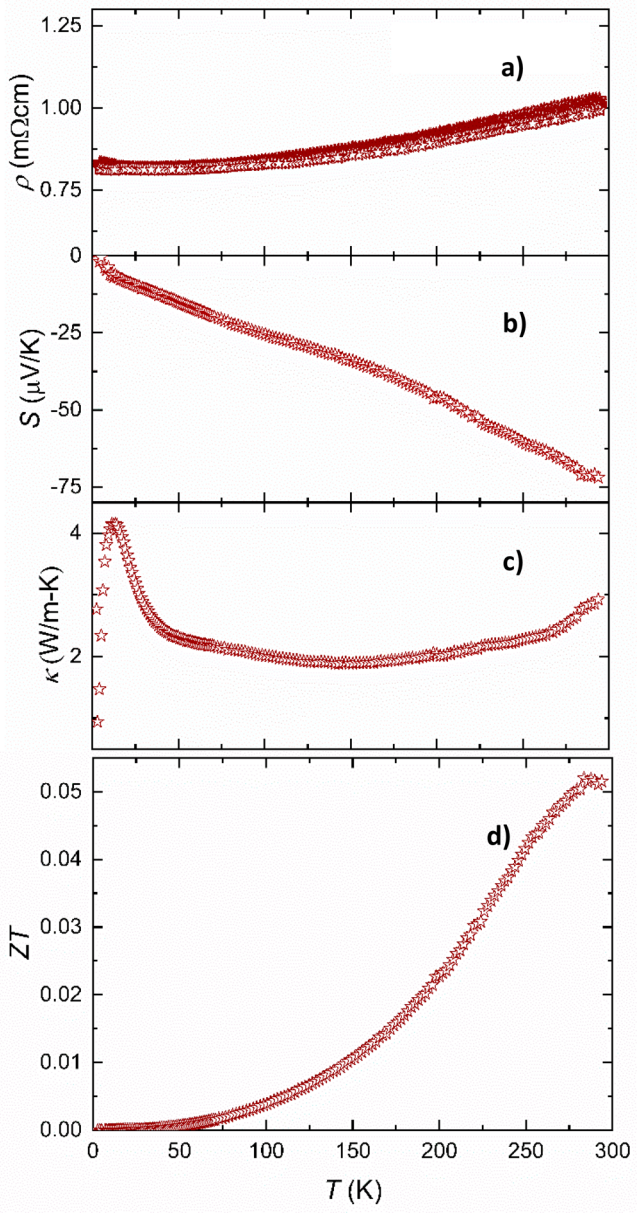

Figure 10. Temperature dependence of transport properties of $Ba_5Yb_{2.26}Mg_{16.74}Si_{12}$; data collected on a single crystal from 2−300 K. (a) Resistivity. (b) Seebeck coefficient. (c) Thermal conductivity and (d) thermoelectric figure of merit.

The temperature dependence of the dimensionless thermoelectric figure of merit ($ZT = S^2T/\rho\kappa$) for $Ba_5Yb_{2.26}Mg_{16.74}Si_{12}$ is shown in Figure 10d. In the low temperature range explored, it has a maximum value of 0.05 at 300 K, which is higher than that of $Ba_{1.9}Ca_{2.4}Mg_{9.7}Si_7$ at the same temperature (0.02 at 300 K). For thermoelectric applications, a ZT value of 1 or higher is desired. However, these materials are likely to have better thermoelectric properties at elevated temperatures, as is seen for $Mg_2Si_{0.4}Sn_{0.6}$ (max ZT of 1.2 at a temperature of 700 K) and $Yb_{14}MnSb_{11}$ (max ZT of ∼1 at a temperature of 1223 K).[2,37] High temperature data reported for the related silicide $Ba_{1.9}Ca_{2.4}Mg_{9.7}Si_7$ (with the $Zr_2Fe_{12}P_7$ structure type) showed a maximum ZT of 0.4 at 900 K.[3] High temperature measurements of thermoelectric properties are needed, but this requires specialized equipment.

Data for $Ba_5Eu_{2.85}Mg_{16.15}Si_{12}$ are shown in Figure 11. The thermal conductivity for this compound is low, with a value of 2.6 W/mK from 150 to 300 K; like the Yb analogue, it exhibits a rise at low temperature and a maximum at 20 K due to reduction of lattice vibrations as the temperature drops. Electrical resistivity is roughly constant at 20 mΩ·cm from 100 to 300 K, higher than that of the ytterbium analogue. Below 10 K, a sharp increase in resistivity occurs. This may be due to the formation of spin clusters in this compound which scatter electrons. It is notable that no long-range magnetic ordering of europium moments is observed for this compound (see Figure 7), although signs of deviations from Curie−Weiss behavior become apparent below 4 K. It is possible that the random distribution of Eu^{2+} ions and resulting variations in local concentrations could cause short-range magnetic ordering, resulting in increased electrical resistivity. Explorations of the low temperature magnetoresistance behavior of this compound may be warranted; $Eu_{7.2}Mg_{15.8}Si_{13}$ was reported to exhibit complex magnetoresistive behavior near its ordering temperature, and strong magnetoresistive effects were noted in other europium-containing Zintl phases including EuMgSn and $EuIn_2Pn_2$ (Pn = P or As).[23,38−40]

The Seebeck coefficient S for $Ba_5Eu_{2.85}Mg_{16.15}Si_{12}$ is positive, indicating that the majority of charge carriers are holes. This is notable, given the relative rarity of p-type thermoelectric materials. Compounds such as Mg_2Si are inherently n-type and need to be doped in order to become p-type. It is unclear whether the p-type behavior of $Ba_5Eu_{2.85}Mg_{16.15}Si_{12}$ is due to incorporation of Eu^{3+} on the europium sites (this is not

https://dx.doi.org/10.1021/acs.cgd.0c00012
Cryst. Growth Des. 2020, 20, 2632−2643

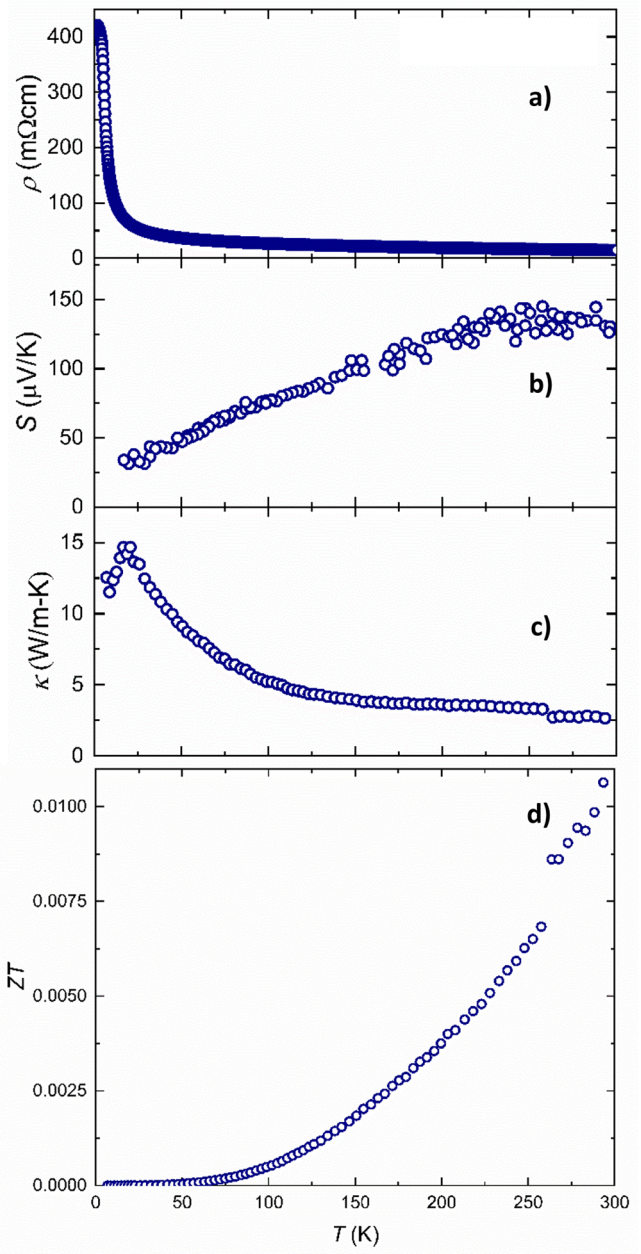

Figure 11. Temperature dependence of transport properties of single crystal $Ba_5Eu_{2.85}Mg_{16.15}Si_{12}$. (a) Resistivity. (b) Seebeck coefficient. (c) Thermal conductivity. (d) Thermoelectric figure of merit.

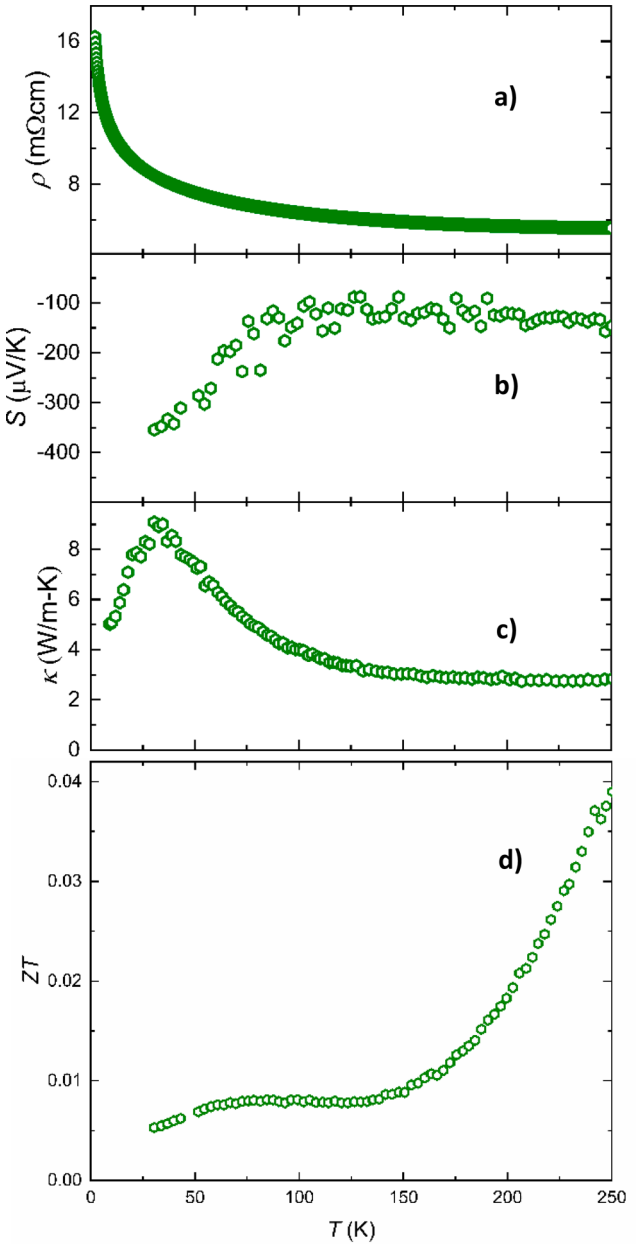

Figure 12. Temperature dependence of transport properties of single crystal $Ba_5Sr_{2.92}Mg_{16.08}Si_{12}$. (a) Electrical resistivity. (b) Seebeck coefficient. (c) Thermal conductivity. (d) Thermoelectric figure of merit.

indicated by the magnetic data) or doping of aluminum on the silicon sites; further work is needed to explore this. The magnitude rises from 30 μV/K at the lowest temperature measured, to +130 μV/K at room temperature.

The temperature dependence of ZT for $Ba_5Eu_{2.85}Mg_{16.15}Si_{12}$ is shown in Figure 11d; it has a maximum value of 0.01 at 300 K. This is lower than the figure of merit of the ytterbium analogue (0.05 at 300 K) and $Ba_{1.9}Ca_{2.4}Mg_{9.7}Si_7$ (0.02 at 300 K). This is likely due to the higher resistivity for the europium analogue, which balances its higher Seebeck coefficient. Again, the value of ZT is expected to be higher at elevated temperature, so high temperature measurements are needed.

Thermoelectric data for $Ba_5Sr_{2.92}Mg_{16.08}Si_{12}$ are shown in Figure 12. The thermal conductivity for this compound is low, with a value of 3 W/mK from 150−300 K; like the Yb and Eu analogues, it exhibits a rise at low temperature and a maximum at 30 K due to reduction of lattice vibrations as the temperature drops. Electrical resistivity shows poor metal behavior, dropping from 16 mΩ·cm at 5 K to 4 mΩ·cm 300 K. The room temperature resistivity is higher than that of the ytterbium analogue, but lower than that of the europium analogue. The negative sign of the Seebeck coefficient S indicates that the dominant charge carriers in $Ba_5Sr_{2.92}Mg_{16.08}Si_{12}$ are electrons. However, S drops in magnitude as temperature rises, from close to −400 μV/K at low temperature to −150 μV/K at 300 K. This may indicate that charge carrier compensation is occurring; electrons dominate at low temperatures, but holes (produced possibly by extrinsic dopants as was seen for the Eu analogue) become increasingly prevalent as the temperature rises. Similar

https://dx.doi.org/10.1021/acs.cgd.0c00012
Cryst. Growth Des. 2020, 20, 2632−2643

behavior was reported for Co_4Sb_{12} skutterudite compounds doped with barium and bismuth.[41,42] The thermoelectric figure of merit ZT for $Ba_5Sr_{2.92}Mg_{16.08}Si_{12}$ (shown in Figure 12d) has a maximum value of 0.04 at 300 K. This is slightly lower than the figure of merit of the ytterbium analogue (0.05 at 300 K), but higher than that of $Ba_{1.9}Ca_{2.4}Mg_{9.7}Si_7$(0.02 at 300 K) and $Ba_5Eu_{2.85}Mg_{16.15}Si_{12}$ (0.01 at 300 K).[12] Again, the value of ZT is expected to be higher at elevated temperatures, so high temperature measurements are needed.

CONCLUSION

Reactions of tetrel elements (Tt = Si, Ge, Sn) with divalent metals (A = Ca, Sr, Ba, Eu, Yb) in Mg/Al flux mixtures have produced a plethora of new complex hexagonal semimetallic tetrelides (Table 3). Given the flexibility toward substitution and the variety of structure types, it is likely that a vast array of additional $(A/Mg)_2Tt$ compounds can be made. Further investigation is needed of the effects of ion size and reaction heating profile to allow for controllable fine-tuning and targeting of specific analogues. Our initial exploration of europium containing analogues reveal intriguing magnetic properties including possible magnetoresistance at low temperature.

The thermoelectric properties of these complex $(A/Mg)_2Tt$ phases show great promise. Both $Ba_5Yb_{2.26}Mg_{16.74}Si_{12}$ and $Ba_5Sr_{2.92}Mg_{16.08}Si_{12}$ have much higher ZT values (0.05 and 0.04) at room temperature than $Ba_{1.9}Ca_{2.4}Mg_{9.7}Si_7$. This is to be expected considering that these compounds have a more complex structure type than $Ba_{1.9}Ca_{2.4}Mg_{9.7}Si_7$ and contain heavier elements, such Sr and Yb. These phases should achieve a much higher ZT value at their maximum temperatures compared to $Ba_{1.9}Ca_{2.4}Mg_{9.7}Si_7$, which has a maximum ZT of 0.4 at 950−1000 K. Tetrelides with the more complex $Ho_6Ni_{20}P_{13}$ and $Ho_{20}Ni_{66}P_{43}$ structure types are likely to have even higher ZT values. These compounds can only be grown from flux reactions at this time; efforts are underway to increase the yields and crystal size of phases such as $Ba_{20}Yb_{4.7}Mg_{61.3}Si_{43}$ for thermoelectric measurements.

ASSOCIATED CONTENT

Accession Codes

CCDC 1958414−1958420, 1958422, 1958425−1958434, and 1958567 contain the supplementary crystallographic data for this paper. These data can be obtained free of charge via www.ccdc.cam.ac.uk/data_request/cif, or by emailing data_request@ccdc.cam.ac.uk, or by contacting The Cambridge Crystallographic Data Centre, 12 Union Road, Cambridge CB2 1EZ, UK; fax: +44 1223 336033.

AUTHOR INFORMATION

Corresponding Author

Susan E. Latturner − *Department of Chemistry and Biochemistry, Florida State University, Tallahassee, Florida 32306, United States;* orcid.org/0000-0002-6146-5333; Email: slatturner@fsu.edu

Authors

Guillermo Vasquez − *Department of Chemistry and Biochemistry, Florida State University, Tallahassee, Florida 32306, United States*

Kaya Wei − *National High Magnetic Field Laboratory and Department of Physics, Florida State University, Tallahassee, Florida 32306, United States*

Eun Sang Choi − *National High Magnetic Field Laboratory and Department of Physics, Florida State University, Tallahassee, Florida 32306, United States*

Ryan Baumbach − *National High Magnetic Field Laboratory and Department of Physics, Florida State University, Tallahassee, Florida 32306, United States*

Complete contact information is available at: https://pubs.acs.org/10.1021/acs.cgd.0c00012

Notes

The authors declare no competing financial interest.

ACKNOWLEDGMENTS

This research was supported by the Division of Materials Research of the National Science Foundation (Grants DMR-14-10214 and DMR-18-08471). This work utilized Scanning Electron Microscope equipment of the Biological Sciences Imaging Resource (BSIR) in the Florida State University Department of Biology; we thank Dr. Eric Lochner for guidance with this instrument. Part of this work was performed at the National High Magnetic Field Laboratory (NHMFL), which is supported by National Science Foundation Cooperative Agreements No. DMR-1157490 and DMR-1644779, the State of Florida, and the Department of Energy.

REFERENCES

(1) Toberer, E. S.; May, A. F.; Snyder, G. J. Zintl Chemistry for Designing High Efficiency Thermoelectric Materials. *Chem. Mater.* **2010**, *22*, 624−634.

(2) Zhang, Q.; He, J.; Zhu, T. J.; Zhang, S. N.; Zhao, X. B.; Tritt, T. M. High Figures of Merit and Natural Nanostructures in $Mg_2Si_{0.4}Sn_{0.6}$ Based Thermoelectric Materials. *Appl. Phys. Lett.* **2008**, *93*, 102109.

(3) Silsby, K.; Sui, F.; Ma, X.; Kauzlarich, S. M.; Latturner, S. E. Thermoelectric Properties of $Ba_{1.9}Ca_{2.4}Mg_{9.7}Si_7$: A New Silicide Zintl Phase with the $Zr_2Fe_{12}P_7$ Structure Type. *Chem. Mater.* **2015**, *27*, 6708−6716.

(4) Bauer, D.; Diamond, D.; Li, J.; Sandalow, D.; Telleen, P.; Wanner, B. *Critical Materials Strategy*; U.S. Department of Energy, 2012. Retrieved May, 28, 2019 from http://energy.gov/sites/prod/files/edg/news/documents/criticalmaterialsstrategy.pdf.

(5) Condron, C. L.; Kauzlarich, S. M.; Nolas, G. S. Structure and Thermoelectric Characterization of $A_xBa_{8-x}Al_{14}Si_{31}$ (A = Sr, Eu) Single Crystals. *Inorg. Chem.* **2007**, *46*, 2556−2562.

(6) Kanatzidis, M. G.; Pöttgen, R.; Jeitschko, W. The Metal Flux: A Preparative Tool for the Exploration of Intermetallic Compounds. *Angew. Chem., Int. Ed.* **2005**, *44*, 6996−7023.

(7) Muret, P; Lefki, K; Nguyen, T T A; Cola, A; Ali, I Band Discontinuities at β-$FeSi_2$/Si Heterojunctions as Deduced from Their Photoelectric and Electrical Properties. *Semicond. Sci. Technol.* **1994**, *9*, 1395−1403.

(8) Okada, S.; Shishido, T.; Ishizawa, Y.; Ogawa, M.; Kudou, K.; Fukuda, T.; LundstrLm, T. MnSi and $MnSi_{2-x}$ Single Crystals Growth by Ga flux Method and Properties. *J. Alloys Compd.* **2001**, *229*, 532−536.

(9) Dalapati, G. K.; Masudy-Panah, S.; Kumar, A.; Tan, C. C.; Ru, H.; Chi, D. Aluminium Alloyed Iron-Silicide/Silicon Solar Cells: A Simple Approach for Low Cost Photovoltaic Technology. *Nat. Publ. Gr.* **2015**, 1−9.

(10) Okada, S.; Yutaka, S.; Fujiwara, K. Molten Metal Flux Growth and Properties of $CrSi_2$. *J. Alloys Compd.* **2004**, *383*, 319−321.

(11) Udono, H.; Nakamori, K.; Takahashi, Y.; Ujiie, Y.; Ohsugi, I. J.; Iida, T. Solution Growth and Thermoelectric Properties of $MnSi_{1.75-x}$. *J. Electron. Mater.* **2011**, *40*, 1165−1170.

(12) Vasquez, G.; Latturner, S. E. Metal Flux Growth of Complex Alkaline Earth/Rare Earth Metal Silicides with a Homologous Series

of Metal Phosphide Structure Types. *Chem. Mater.* **2018**, *30*, 6478−6485.
(13) *SAINT*, Version 6.02a; Bruker AXS, Inc.: Madison, WI, 2000.
(14) Sheldrick, G. M. *SHELXTL NT/2000*, Version 6.1; Bruker AXS, Inc.: Madison, WI, 2000.
(15) You, A.; Be, M. A. Y.; In, I. Technique for Thermal Conductivity Measurements for Organic Materials over a Wide Temperature Range. *Rev. Sci. Instrum.* **2004**, 75.
(16) Vasquez, G.; Huq, A.; Latturner, S. E. *In situ* Diffraction studies of the growth of Ba/Yb/Mg/Si intermetallics in Mg/Al flux. *Inorg. Chem.* **2019**, *58*, 8111−8119.
(17) Steinwand, S. J.; Hurng, W. M.; Corbett, J. D. The Zintl Phases $Sr_{2.2}Mg_{11.8}Ge_7$ and $Sr_5Mg_{19}Ge_{12}$. *J. Solid State Chem.* **1991**, *94*, 36−44.
(18) Zürcher, F.; Nesper, R. Cationic Channels with Partial Anion Occupation in the Zintl Phases $Ba_2Mg_{12}Ge_{7.33}$ and $Ba_6Mg_{17.4}Li_{2.6}Ge_{12}O_{0.64}$. *ZAAC* **2002**, *628*, 1581−1589.
(19) Kubeta. Christof Maximilian. *Synthese, Strukturen und Eigenschaften neuer mehrkomponentiger Silicide und Germanide der Seltenerdmetalle*. Justus Liebig-Universität Giessen. Doctor of Philosophy Dissertation, 2004.
(20) Slabon, A.; Cuervo-Reyes, E.; Kubata, C.; Mensing, C.; Nesper, R. Exploring the Borders of the Zintl-Klemm Concept: on the Isopunctual Phases $Eu_{(5+x)}Mg_{(18-x)}Ge_{13(x=0.1)}$ and $Eu_8Mg_{16}Ge_{12}$. *Z. Anorg. Allg. Chem.* **1950**, 2020−2028.
(21) Nesper, R.; Wengert, S.; Zuercher, F.; Currao, A. Electronic Variations in Carbonate- and Phosphine-related 24- and 26-Electron E_4 clusters of Silicon and Germanium. *Chem. - Eur. J.* **1999**, *5*, 3382−3389.
(22) Whalen, J. B. *Hydrogen Storage and Electronic Characterization of Magnesium-Based Intermetallics: Exploratory Flux Synthesis for Advanced Materials*. Doctor of Philosophy Dissertation, Florida State University, 2009.
(23) Slabon, A.; Mensing, C.; Kubata, C.; Cuervo-Reyes, E.; Nesper, R. Field-induced Inversion of the Magnetoresistive Effect in the Zintl Phase $Eu_{5+x}Mg_{18-x}Si_{13(x=2.2)}$. *Angew. Chem., Int. Ed.* **2013**, *52*, 2122−2125.
(24) Pivan, J. Y.; Guerin, R.; Sergent, M. A New Classification Scheme to Describe and Predict Structure Types in Pnictide and Silicide Chemistry. *J. Solid State Chem.* **1987**, *68*, 11−21.
(25) Prots, Y. M.; Jeitschko, W. Lanthanum Nickel Silicides with the General Formula $La_{(n+1)(n+2)}$ $Ni_{n(n-1)+2}Si_{n(n+1)}$ and Other Series of Hexagonal Structures with Metal: Metalloid Ratios Close to 2:1. *Inorg. Chem.* **1998**, *37*, 5431−5438.
(26) Eisenmann, B.; Schaefer, H.; Weiss, A. Der Uebergang vom "geordneten" Anti-Pb C_{l2}-Gitter zum Anti-PbFCl-Gitter: Ternaere Phasen ABX der Erdalkalimetalle mit Elementen der 4. Hauptgruppe (A = Ca, Sr, Ba; B = Mg; X = Si, Ge, Sn, Pb). *Z. Anorg. Allg. Chem.* **1972**, *391*, 241−254.
(27) Evers, J.; Oehlinger, G.; Weiss, A. Solid solutions $M_{1-x}Sr_xSi_2$ (M = Ca, Eu, Ba) and $BaSi_{2-y}Ge_y$ with $SrSi_2$-type structure. *J. Less-Common Met.* **1980**, *69*, 399−402.
(28) Liu, S.; Corbett, J. D. Synthesis, Structure, and Properties of Four Ternary Compounds Ca Sr Tt, Tt = Si, Ge, Sn, Pb. *J. Solid State Chem.* **2006**, *179*, 830−835.
(29) Saravanan, R.; Robert, M. C. Local Structure of the Thermoelectric Material Mg_2Si Using XRD. *J. Alloys Compd.* **2009**, *479*, 26−31.
(30) Vaughey, J. T.; Miller, G. J.; Gravelle, S.; Leon Escamilla, E. A.; Corbett, J. D. Synthesis, Structure, and Properties of $BaGe_2$: A Study of Tetrahedral Cluster Packing and Other Three-Connected Nets in Zintl Phases. *J. Solid State Chem.* **1997**, *133*, 501−507.
(31) Pani, M.; Palenzona, A. The Phase Diagram of the Yb-Ge System. *J. Alloys Compd.* **2003**, *360*, 151−161.
(32) Merlo, F.; Fornasini, M. L. CrB-type Equiatomic Compounds of Europium, Ytterbium and Alkaline-Earth Metals with Si, Ge, Sn, Pb. *J. Less-Common Met.* **1967**, *13*, 603−610.
(33) Zaitsev, V. K.; Fedorov, M. I.; Gurieva, E. A.; Eremin, I. S.; Konstantinov, P. P.; Samunin, A. Y.; Vedernikov, M. V. Highly Effective $Mg_2Si_{1-x}Sn_x$ Thermoelectrics. *Phys. Rev. B: Condens. Matter Mater. Phys.* **2006**, *74*, 1−5.
(34) Bourgeois, J.; Lorraine, D.; Aiguillettes, B.; Tobola, J.; Wiendlocha, B.; Lorraine, D.; Aiguillettes, B.; Zwolenski, P.; Lorraine, D.; Aiguillettes, B. Study of Electron, Phonon and Crystal Stability versus Thermoelectric Properties in Mg_{2X} (X = Si, Sn) Compounds and their alloys. *Funct. Mater. Lett.* **2013**, *6*, 1−14.
(35) Kim, H. S.; Kikuchi, K.; Itoh, T.; Iida, T.; Taya, M. Design of Segmented Thermoelectric Generator Based on Cost-Effective and Light-Weight Thermoelectric Alloys Design of Segmented Thermoelectric Generator Based on Cost-Effective and Light-Weight Thermoelectric Alloys. *Mater. Sci. Eng., B* **2014**, *185*, 45−52.
(36) You, A.; Be, M. A. Y.; In, I. Thermoelectric Properties of Semimetallic (Zr, Hf) CoSb half-Heusler Phases. *J. Appl. Phys.* **2008**, *88*, 1952−1955.
(37) Grebenkemper, J. H.; Hu, Y.; Barrett, D.; Gogna, P.; Huang, C. K.; Bux, S. K.; Kauzlarich, S. M. High Temperature Thermoelectric Properties of $Yb_{14}MnSb_{11}$ Prepared from Reaction of MnSb with the Elements. *Chem. Mater.* **2015**, *27*, 5791−5798.
(38) Ma, X.; Lu, J.; Whalen, J. B.; Latturner, S. E. Flux growth and magnetoresistance behavior of rare earth Zintl phase EuMgSn. *Inorg. Chem.* **2013**, *52*, 3342−3348.
(39) Jiang, J.; Kauzlarich, S. M. Colossal magnetoresistance in a rare earth Zintl compound with a new structure type: $EuIn_2P_2$. *Chem. Mater.* **2006**, *18*, 435.
(40) Goforth, A. M.; Klavins, P.; Fettinger, J. C.; Kauzlarich, S. M. Magnetic properties and negative colossal magnetoresistance of the rare earth Zintl phase $EuIn_2As_2$. *Inorg. Chem.* **2008**, *47*, 11048−11056.
(41) Chen, L. D.; Kawahara, T.; Tang, X. F.; Goto, T.; Hirai, T.; Dyck, J. S.; Chen, W.; Uher, C. Anomalous barium filling fraction and n-type thermoelectric performance of $Ba_yCo_4Sb_{12}$. *J. Appl. Phys.* **2001**, *90*, 1864−1868.
(42) Mallik, R. C.; Anbalagan, R.; Raut, K. K.; Bali, A.; Royanian, E.; Bauer, E.; Rogl, G.; Rogl, P. Thermoelectric properties of Bi-added Co_4Sb_{12} skutterudites. *J. Phys.: Condens. Matter* **2013**, *25*, 105701.

https://dx.doi.org/10.1021/acs.cgd.0c00012
Cryst. Growth Des. 2020, 20, 2632−2643